Title

Associations Between MRI-Assessed Locus Coeruleus Integrity and Cortical Gray Matter Microstructure

Journal

Cerebral Cortex, 32(19)

ISSN

1047-3211

Authors

Elman, Jeremy A

Puckett, Olivia K

Hagler, Donald J

et al.

Publication Date

2022-09-19

DOI

10.1093/cercor/bhab475

Peer reviewed

OXFORD

Cerebral Cortex, 2022, **32**, 4191–4203
https://doi.org/10.1093/cercor/bhab475
Advance access publication date 31 December 2021
Original Article

Associations between MRI-assessed locus coeruleus integrity and cortical gray matter microstructure

Jeremy A. Elman[1,2,*], Olivia K. Puckett[1,2], Donald J. Hagler Jr[3], Rahul C. Pearce[1,2], Christine Fennema-Notestine[1,3], Sean N. Hatton[2,4], Michael J. Lyons[5], Linda K. McEvoy[3,6], Matthew S. Panizzon[1,2], Emilie T. Reas[4], Anders M. Dale[3,4], Carol E. Franz[1,2], William S. Kremen[1,2,7]

[1]Department of Psychiatry, University of California San Diego, La Jolla, CA 92093, USA,
[2]Center for Behavior Genetics of Aging, University of California San Diego, La Jolla, CA 92093, USA,
[3]Department of Radiology, University of California San Diego, La Jolla, CA 92093, USA,
[4]Department of Neurosciences, University of California San Diego, La Jolla, CA 92093, USA,
[5]Department of Psychological and Brain Sciences, Boston University, Boston, MA 02215, USA,
[6]Herbert Wertheim School of Public Health and Human Longevity Science, University of California San Diego, La Jolla, CA 92093, USA,
[7]Center of Excellence for Stress and Mental Health, VA San Diego Health Care System, La Jolla, CA 92161, USA
*Address correspondence to Jeremy A. Elman, Department of Psychiatry, University of California San Diego, 9500 Gilman Dr. (MC0738), La Jolla, CA 92093, USA. Email: jaelman@health.ucsd.edu.

The locus coeruleus (LC) is one of the earliest sites of tau pathology, making it a key structure in early Alzheimer's disease (AD) progression. As the primary source of norepinephrine for the brain, reduced LC integrity may have negative consequences for brain health, yet macrostructural brain measures (e.g. cortical thickness) may not be sensitive to early stages of neurodegeneration. We therefore examined whether LC integrity was associated with differences in cortical gray matter microstructure among 435 men (mean age = 67.5; range = 62–71.7). LC structural integrity was indexed by contrast-to-noise ratio (LC_{CNR}) from a neuromelanin-sensitive MRI scan. Restriction spectrum imaging (RSI), an advanced multi-shell diffusion technique, was used to characterize cortical microstructure, modeling total diffusion in restricted, hindered, and free water compartments. Higher LC_{CNR} (greater integrity) was associated with higher hindered and lower free water diffusion in multiple cortical regions. In contrast, no associations between LC_{CNR} and cortical thickness survived correction. Results suggest lower LC integrity is associated with patterns of cortical microstructure that may reflect a reduction in cytoarchitectural barriers due to broader neurodegenerative processes. These findings highlight the potential utility for LC imaging and advanced diffusion measures of cortical microstructure in assessing brain health and early identification of neurodegenerative processes.

Key words: Alzheimer's disease; aging; diffusion; neuromelanin MRI; restriction spectrum imaging.

The locus coeruleus (LC) is a small brainstem structure that serves as the brain's primary source of norepinephrine (NE) (Berridge and Waterhouse 2003). It plays an important neuromodulatory role with widespread projections throughout the brain (Aston-Jones and Cohen 2005; Mather et al. 2016). Although often linked to arousal and vigilance (Aston-Jones et al. 1994; Rajkowski et al. 1994; Samuels and Szabadi 2008; Sara and Bouret 2012), the LC is also involved in higher order cognitive processes such as memory (Sara 2009, 2015; Mather et al. 2016; Breton-Provencher et al. 2021). A number of autopsy studies have demonstrated clinicopathologic correlations in Alzheimer's disease (AD) involving the LC. For example, neurofibrillary tangles and tissue loss in the LC correlate with premortem disease duration and symptom severity (Bondareff et al. 1987; German et al. 1987; German et al. 1992; Grudzien et al. 2007; Wilson et al. 2013; Kelly et al. 2017; Theofilas et al. 2017). In fact, the LC may be one of the earliest sites of abnormal tau pathology (Braak et al. 2011), so assessing its structure and function holds great potential for early identification of AD risk.

Despite its small size, LC dysfunction may have widespread and serious consequences. The LC-NE system contributes to the maintenance of brain health through multiple routes (Mather and Harley 2016; Matchett et al. 2021). LC-synthesized NE plays an important role in regulating neuroinflammation, and therefore, its reduction can result in a heightened inflammatory state that leads to neurodegeneration (Feinstein et al. 2002; Heneka et al. 2010; Jardanhazi-Kurutz et al. 2011; Ransohoff 2016). Damage to the LC has also been shown to increase the accumulation of AD pathology as well as the inflammatory response to this pathology (Heneka et al. 2002; Weinshenker 2018). NE also has neuroprotective effects such as promoting the expression of growth factors critical for cell survival and contributing to efficient neural functioning

Received: August 24, 2021. **Revised:** November 17, 2021. **Accepted:** November 22, 2021

(Chen and Russo-Neustadt 2007; Robertson 2013). Therefore, loss of LC integrity and subsequent NE depletion may leave the brain more vulnerable to insults that accumulate throughout the lifespan.

Studying the LC in vivo has been especially difficult due to its small size and because it is not visible on standard T1-weighted MRI sequences commonly used to examine brain structure. However, the development of novel MRI sequences has made imaging the LC possible (Sasaki et al. 2006; Liu et al. 2017; Betts et al. 2019b; Kelberman et al. 2020). The exact basis of this signal is unclear, but it may be related to signal from neuromelanin, a metabolite of NE that binds to metals and is highly concentrated in the LC (Betts et al. 2019b). It may also reflect the ratio of macromolecular to free water ratio in the LC, with decreasing values indicating reduced density or shrinkage of noradrenergic neurons (Priovoulos et al. 2020).

These developments have prompted increased focus on using higher signal contrast as a measure of greater LC integrity (Keren et al. 2015), and thus as an early indicator of AD pathophysiological processes. Higher LC integrity has been linked to better performance across multiple cognitive domains (Hammerer et al. 2018; Dahl et al. 2019; Elman et al. 2021), potentially due to its more global role of modulating neural activity in cortical regions that support these processes. Reduced MRI-assessed LC integrity has been observed in individuals with AD (Betts et al. 2019a) and those with mild cognitive impairment (MCI) (Takahashi et al. 2015; Elman et al. 2021). A recent study incorporating LC imaging and autopsy data found that age-related changes in LC_{CNR} are primarily driven by AD pathology, and that associations between LC_{CNR} and AD-related cognitive decline are mediated by medial temporal lobe tau burden (Jacobs et al. 2021). The authors conclude that LC_{CNR} may be used as a proxy for early tau deposition in the LC. Taken together, these findings support the use of LC imaging to better understand factors that contribute to cognitive and brain health and risk for AD.

The irreversible nature of brain atrophy lends great importance to early detection of neurodegenerative processes. A study by Bachman et al. (2021) found that LC_{CNR} was associated with cortical thickness in older adults. However, brain changes in early disease stages are likely to be quite subtle and may be difficult to detect with commonly used metrics such as cortical thickness or volume in some individuals. Diffusion MRI (dMRI) may provide a more sensitive approach to detecting microstructural changes in cell bodies and axonal fibers that precede macrostructural changes evident on standard T1-weighted images. For example, cortical mean diffusivity (MD) has been proposed as a useful measure for identifying early AD-related atrophy (Weston et al. 2015). Cortical MD was also shown to correlate with predicted symptom onset in carriers of familial AD mutations even after controlling for cortical thickness (Weston et al. 2020), indicating that it provides independent information. Furthermore, an AD brain signature based on MD in selected AD-related cortical regions of men in their 50s significantly improved prediction of 12-year progression to MCI over and above age and AD polygenic risk whereas a cortical thickness signature did not (Williams et al. 2021).

One shortcoming of conventional dMRI (e.g. diffusion tensor imaging or DTI) is its inability to delineate complex microstructural organization at the voxel level, especially in gray matter, where multiple cytoarchitectural features (i.e. cell bodies, neurites, and CSF) may exist within each voxel due to the more broadly dispersed nature of gray matter components. Advanced multi-shell diffusion techniques such as restriction spectrum imaging (RSI) have allowed for better characterization of this complex microstructural architecture. RSI utilizes a multi-compartment, multi-directional model, measuring contributions to the diffusion-weighted signal along a spectrum of length scales, from restricted to hindered to free diffusion (White et al. 2013a; White et al. 2014). The restricted component may be sensitive to intracellular diffusion, detecting variation in small cell and neurite density, as well as axonal myelination or thin glial processes. The hindered component may reflect diffusion in the extracellular compartment or the density of large neuronal or glial cell bodies in gray matter. The isotropic free component models free water diffusion, reflecting the volume fraction of CSF in each voxel, which may increase as cellular boundaries along the cortical mantle break down. This method additionally models crossing fibers, which may manifest as artificially reduced anisotropic diffusion in conventional DTI. RSI metrics have been found to differentiate cognitively normal individuals from those with MCI or AD, as well as to show associations with AD pathology and memory performance (Reas et al. 2017; Reas et al. 2020).

The neuromodulatory and neuroprotective effects of the LC-NE system mean that reduced LC integrity should have negative consequences for neural integrity in widespread cortical regions innervated by this structure. In vivo imaging of the LC allows for early monitoring of a key structure involved early in the AD process. RSI further allows for detection of subtle microstructural change that may not be evident using standard MRI techniques that focus on macrostructure such as cortical thickness. We examine the relationship between these measures of LC and cortical integrity in a sample of community-dwelling men aged 62–71. Linking these putative measures of LC and cortical integrity would provide evidence that these techniques may provide sensitive measures for identifying early signs of neurodegeneration.

Methods

Participants

Participants were from wave 3 of the Vietnam Era Twin Study of Aging (VETSA) project (Kremen et al. 2019).

VETSA participants comprise a national, community-dwelling sample of male–male twins who are similar to American men in their age range with respect to health and lifestyle characteristics based on Center for Disease Control and Prevention data (Schoenborn and Heyman 2009). All served in the military service sometime between 1965 and 1975, but nearly 80% reported no combat exposure. Additionally, prevalence of traumatic brain injury (TBI) in the full VETSA sample (31.4%) is similar to a Colorado community sample (42.5%) (Whiteneck et al. 2016) and only 1.2% of TBI in the included sample was combat related. Most TBIs were mild and occurred an average of about 40 years prior to the study (Kaup et al. 2019). Participants took the Armed Forces Qualification Test (AFQT) (Uhlaner and Bolanovich 1952) upon induction into the military (approximately 20 years of age) and during their VETSA wave 3 assessment. The AFQT has a high correlation with other tests of general cognitive ability (Lyons et al. 2009; Lyons et al. 2017). Classification of mild cognitive impairment (MCI) was based on the Jak-Bondi criteria (Jak et al. 2009).

The VETSA 3 MRI component included 525 participants using standard MRI exclusion criteria (e.g. no metal in the body). Participants were included in the study if they had useable data for all imaging modalities. LC imaging data were acquired for 487 participants, but data from 6 participants were excluded due to excessive motion. An additional 46 participants were excluded who did not have useable cortical thickness and diffusion data, leaving an analytic sample size of 435. The sample had a mean age of 67.5 years (range 62–71; SD = 2.6), a mean education of 14 (SD = 2.1) years and was primarily Caucasian (90%). Participants had a mean BMI of 29.09 (SD = 4.25), a mean score of 6.84 (SD = 6.90) on the Center for Epidemiological Studies-Depression scale (Radloff 1977), 22.5% had diabetes, 56.3% had hypertension, and 14% were classified as having MCI. The mean AFQT percentile score for participants was 60.82 (SD = 21.98) at age 20 and 54.32 (SD = 21.47) during the VETSA wave 3 assessment. These scores are comparable to a mean IQ score of approximately 104 and 102, respectively.

The study was approved by the Institutional Review Board at the University of California, San Diego (UCSD) and written informed consent was obtained from all study participants.

MRI Acquisition

Images were acquired with two GE 3 T Discovery 750× scanners (GE Healthcare, Waukesha, WI, USA) with eight-channel phased array head coils. The imaging protocol included a sagittal 3D fast spoiled gradient echo (FSPGR) T_1-weighted (T1w) volume optimized for maximum gray/white contrast (TE = 3.164 ms, TR = 8.084 ms, TI = 600 ms, flip angle = 8°, matrix = 256 × 192, in-plane resolution = 1 × 1 mm, slice thickness = 1.2 mm, slices = 172). The LC was imaged with an axial fast spin-echo T1-weighted image (TR = 600 ms; TE = 14 ms; flip angle = 90^0; matrix = 512 × 320; FOV = 220 mm; pixel size = 0.42 × 0.68 mm; 10 slices; slice thickness = 2.5 mm; interslice gap = 1 mm). Diffusion data were acquired with a multi-shell diffusion-weighted scan (54-directions, b values = [0 (×3), 666 (×6), 1333 (×15), 2666 (×15), 4000 (x15)] s/mm^2, integrated with a pair of $b = 0$ images with opposite phase-encode polarity, TR = 6600 ms, TE = 81.1 ms, matrix = 96 × 96, in-plane resolution = 2.5 × 2.5 mm, slice thickness = 2.5 mm, 54 slices).

Structural MRI Processing

Structural MR images were processed as described previously (Kremen et al. 2010) using the FreeSurfer software package (Dale et al. 1999; Fischl et al. 1999; Fischl and Dale 2000; Fischl et al. 2004b). Briefly, this involves correction of distortion due to gradient nonlinearity (Jovicich et al. 2006), image intensity normalization, rigid registration into standard orientation with 1 mm isotropic voxel size, removal of non-brain tissue, and segmentation of the subcortical white matter and deep gray matter volumetric structures (Fischl et al. 2002; Fischl et al. 2004a). Boundaries between GM, WM, and cerebral spinal fluid (CSF) were defined and the cortical surface was then divided into 66 distinct regions (33 per hemisphere) according to the Desikan-Killiany atlas (Desikan et al. 2006). Surface area and mean cortical thickness was calculated for each ROI. All raw and processed images were visually inspected for quality. White matter and brain masks were manually edited as necessary in alignment with standard, objective editing rules.

LC MRI Processing

Each image was manually marked by two of four experienced raters according to methods described in detail previously (Elman et al. 2021). Briefly, signal intensities were derived from manually marked regions of interest (ROIs) on three axially-oriented slices corresponding to rostral, middle, and caudal LC. On each slice, a 3-mm^2-voxel crosshair-shaped ROI was placed over left and right LC and a 10-mm^2 square reference ROI was placed in the pontine tegmentum (PT). Mean signal was then extracted from each ROI and values from left and right LC were averaged for each slice. LC contrast-to-noise ratio (LC_{CNR}) values were calculated for each slice as $LC_{CNR} = (LC_{intensity}—PT_{intensity})/PT_{intensity}$. Higher LC_{CNR} values are thought to reflect greater LC structural integrity (Keren et al. 2015). Extant literature suggests that the rostral and middle portions of the LC are more prone to age- and AD-related degeneration than more caudal, cerebellar-projecting portions (German et al. 1992; Betts et al. 2019b). Therefore, the LC_{CNR} values from the two rostral-most marked slices were averaged (LC_{CNR} hereafter refers to rostral/middle LC unless otherwise noted). Each participant image was marked by two raters, and the rostral/middle LC_{CNR} values was averaged across raters to obtain the final LC_{CNR} for each participant. We previously showed that there was good inter-rater reliability on this measure (ICC = 0.87) (Elman et al. 2021).

Exploratory analyses were conducted to examine the impact of methodological choices for calculating LC_{CNR}. We additionally calculated the following LC_{CNR} values: i) LC_{CNR} corresponding to left and right LC separately, ii) LC_{CNR} taken from the caudal LC slice, and iii) LC_{CNR} taken from the slice with the highest CNR across all slices (peak LC_{CNR}). When extracting the maximum value from each LC ROI, the resulting LC_{CNR} was highly correlated with LC_{CNR} derived from taking the mean ROI value ($r > 0.968$ on all slices). Therefore, we use mean values in all analyses.

Diffusion MRI Processing

dMRI images were pre-processed as previously described (Elman et al. 2017b). Images were corrected for B_0 susceptibility (Chang and Fitzpatrick 1992; Morgan et al. 2004; Holland et al. 2010) eddy current distortions (Zhuang et al. 2006), gradient nonlinearity (Jovicich et al. 2006), and head motion (Hagler Jr et al. 2009). T_2-weighted $b = 0$ images were registered to T_1-weighted structural images and registrations were reviewed manually for quality. Diffusion-weighted images were resampled into a standard orientation with 2-mm isotropic resolution; the number of resampling steps was reduced by combining this with the motion correction. Cubic interpolation was used for all resampling steps.

Several measures related to microstructural tissue properties were calculated using RSI (White et al. 2013a; White et al. 2013b; White et al. 2014). We use RSI to model mixtures of "restricted," "hindered," and "free" diffusion within individual voxels. The signal fractions representing restricted and hindered diffusion were modeled as fourth-order spherical harmonic, fiber orientation density (FOD) functions. For both fractions, the longitudinal diffusion is modeled as 1×10^{-3} mm^2/s. For the restricted fraction, transverse diffusion is modeled as 0. For the hindered fraction, transverse diffusion is modeled as 0.9×10^{-3} mm^2/s. The free water fraction was modeled as isotropic diffusion with an apparent diffusion coefficient (ADC) of 3.0×10^{-3} mm^2/s. Measures derived from this RSI model fit included restricted normalized isotropic, restricted normalized directional, restricted normalized total, hindered normalized isotropic, hindered normalized directional, hindered normalized total, and free normalized isotropic. These normalized metrics are calculated by taking the norm (square root of the sum of squares) of model fit parameters for a given signal fraction (e.g. restricted, hindered, free) and dividing by the norm of all model fit parameters, which is equivalent to the fitted $b = 0$ signal intensity. These normalized RSI measures are unitless and range from 0 to 1.

The RSI-derived measures described above and previously (Reas et al. 2017; Reas et al. 2020) are normalized signal fractions. Some type of normalization is necessary to account for arbitrary variation in overall intensity scaling across subjects as well as intensity inhomogeneity related to distance from the imaging coils. Normalizing in this way, however, introduces negative correlations between signal fractions. For example, because the square of the normalized signal fractions must sum to one, an increase in the normalized free fraction will necessarily be accompanied by decreases in the normalized restricted or hindered fractions.

To avoid this confounding negative linkage between the estimated signal fractions and to determine whether associations may be driven by one component, we additionally calculated unnormalized versions of each measure. We calculated unnormalized signal fractions as the norm of squared model fit parameters for a given signal fraction. To account for the between-subject variation in signal intensity, as well as intensity inhomogeneity, we pre-normalized the dMRI volumes using a smoothly varying bias field, estimated using sparse spatial smoothing and white matter segmentation, with the simplifying assumption of uniform $b = 0$ intensity values within white matter (Hagler Jr et al. 2019). Bias corrected images were scaled so that white matter intensities will have an average value of 1000. The white matter segmentation used to constrain the sparse spatial smoothing was derived from the T1w volume and resampled into registration with the dMRI volume. Registration of the average $b = 0$ volume to the T1w volume used coarse registration to modality-specific atlas brains followed by fine registration using mutual information. Outlier voxels, defined as voxels in the white matter mask with high $b = 0$ intensity, were removed from the white matter mask to prevent slight inaccuracies in the initial white matter mask from causing poor bias field estimation in those regions with outlier intensities in voxels labeled as white matter (e.g. voxels that contain CSF). The removal of outlier voxels from the white matter mask was done iteratively and was limited to the outer band (~1 cm) of white matter.

Diffusion metrics were mapped to the cortical surface as previously described (Elman et al. 2017b). To minimize the effects of partial voluming and regional variations in cortical thickness, this approach takes a weighted average of multiple samples across the cortical ribbon based on the proportion of gray matter at each sampling location. Vertex-wise estimates of each metric were summarized for each ROI and left and right hemispheres were averaged for a total of 33 bilateral ROI values. We focus on measures of total restricted and hindered diffusion to capture oriented and isotropic diffusion which are both relevant in cortical gray matter, as well as free water. Exploratory analyses were conducted on left and right hemisphere ROIs to explore laterality effects.

Statistical Analysis

Linear mixed effects models were run using the lme4 package (Bates et al. 2015) in R v4.0.5 (R Core Team 2017) to examine cortical thickness and the RSI metrics of total restricted, total hindered, and free water diffusion in each of the 33 cortical ROIs as dependent variables and LC_{CNR} as the independent variable. All models included age and scanner as covariates. Family ID was included as

a random intercept to account for the non-independence of twin pairs. Degrees of freedom, t-statistics, and significance were calculated using the Satterthwaite method as implemented in the package lmerTest (Kuznetsova et al. 2017). We then conducted analyses using the unnormalized versions of total restricted, total hindered, and free water diffusion to provide further information regarding whether one component may be driving observed associations with normalized measures. We corrected for multiple comparisons using the Li and Ji method of FDR adjustment (Li and Ji 2005). ROI results were plotted with the ggseg package (Mowinckel and Vidal-Piñeiro 2020).

Exploratory analyses were run to examine the regional specificity of effects and facilitate comparison with previous studies. Laterality effects of the LC were explored by testing associations of left and right LC_{CNR} separately. Laterality effects in cortex were explored by testing associations of rostral/middle LC_{CNR} with left and right cortical ROIs separately. To facilitate comparisons with previous studies, associations were re-run replacing the rostral/middle LC_{CNR} value with the LC_{CNR} taken from the slice with the highest CNR across all slices (i.e. peak LC_{CNR}). We examined whether effects were regionally specific within the LC by testing associations with LC_{CNR} from the caudal-most slice. Finally, we examined whether associations were specific to the LC in general by using bilateral hippocampal volume as the region of interest instead of rostral/middle LC_{CNR}.

Data Availability

VETSA data are publicly available, with restrictions. Information regarding data access can be found at our website: http://medschool.ucsd.edu/som/psychiatry/research/VETSA.

Results

Associations between LC_{CNR} and RSI

There were nominally significant associations between LC_{CNR} and restricted signal fraction in the rostral and caudal anterior cingulate but neither survived correction for multiple comparisons (Fig. 1A; Table 1). In contrast, several regions showed positive associations that survived correction in which higher LC_{CNR} was related to higher hindered signal fraction, including inferior temporal, superior temporal, lateral and medial parietal, and lateral orbitofrontal cortices (Fig. 1B; Table 1). Higher LC_{CNR} was associated with lower free water signal fraction in a subset of regions that were significantly associated with hindered diffusion (Fig. 1C; Table 1). However, the effects were somewhat weaker and less extensive in the temporo-parietal regions.

To determine whether associations with normalized metrics were primarily driven by one component, we examined associations between LC_{CNR} and unnormalized versions of the RSI metrics. In contrast to the normalized metrics, there were no significant associations with free water. Higher LC_{CNR} was associated with higher hindered diffusion in many cortical regions, with more a more extensive pattern of associations surviving correction compared to that seen with the normalized metric (Fig. 2; Table 2). These results suggest that the associations with the normalized metrics were driven by the hindered component.

Associations between LC_{CNR} and Cortical Thickness

The association between LC_{CNR} and cortical thickness was nominally significant ($P < 0.05$) in the fusiform gyrus and frontal pole, with higher LC integrity associated with thicker cortex (Fig. 1D). However, neither of these regions survived FDR-correction.

Regional Specificity of Associations

Exploratory analyses were run to explore regional specificity and for comparison to other studies. We focus on associations with cortical thickness (for comparison with previous studies) and unnormalized hindered diffusion (the RSI metric showing significant associations with the LC). We explored whether associations differed between left and right LC. Neither left nor right LC_{CNR} showed significant associations with cortical thickness. Right LC_{CNR} did show more extensive associations with unnormalized hindered diffusion that survived correction compared with left LC_{CNR} (Supplemental Fig. S1). Examining unthresholded results suggests that right LC_{CNR} associations were stronger, but the spatial patterns were similar. The association of bilateral rostral/middle LC_{CNR} was similar for left and right hemisphere cortical ROIs. That is, there were no significant associations with cortical thickness and widespread associations with unnormalized hindered diffusion. Except for a small number of ROIs in temporo-parietal cortex, the pattern of results was broadly similar in left and right hemisphere (Supplemental Fig. S2).

LC_{CNR} from the caudal LC did not show any significant associations with cortical thickness or RSI. Across all raters and images, the slice with peak LC_{CNR} was on the middle slice on 50% of markings, the rostral slice 39%, and caudal slice 11%. Peak LC_{CNR} was not associated with cortical thickness but showed similar yet attenuated associations with unnormalized hindered diffusion compared to LC_{CNR} from the rostral/middle LC. Although the spatial pattern of association was similar, ROIs surviving correction for multiple comparisons were more restricted to anterior frontal and temporal cortices (Supplemental Fig. S3).

Finally, we investigated whether significant associations were specific to the LC or representative of global neurodegeneration by examining association with mean bilateral hippocampal volume. We found widespread associations between hippocampal volume and unnormalized hindered diffusion. However, when including both hippocampal volume and rostral/middle LC_{CNR} in the same model, associations for each remained

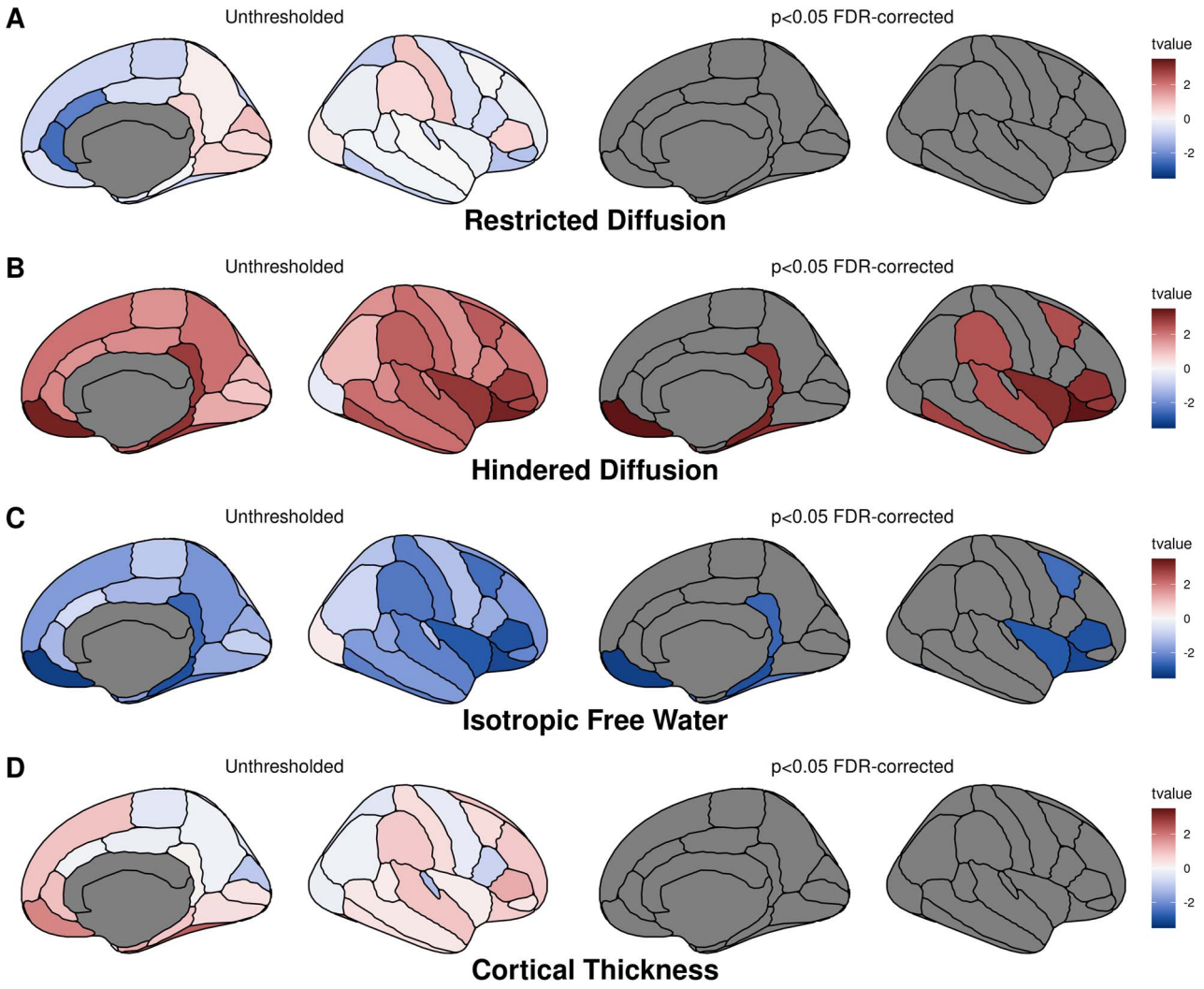

Fig. 1. Regional associations of LC_{CNR} with cortical macrostructure and microstructure. Locus coeruleus contrast-to-noise ratio (LC_{CNR}) was used as in independent variable with cortical thickness or normalized RSI metrics as dependent variable across ROIs defined by the Desikan-Killiany atlas. Left and right hemispheres were averaged for each ROI. Unthresholded t-value maps are presented on the left, and significant regions ($P < 0.05$) surviving FDR-correction are presented on the right for each metric. Visualizations created with the R package *ggseg* (Mowinckel and Vidal-Piñeiro 2020).

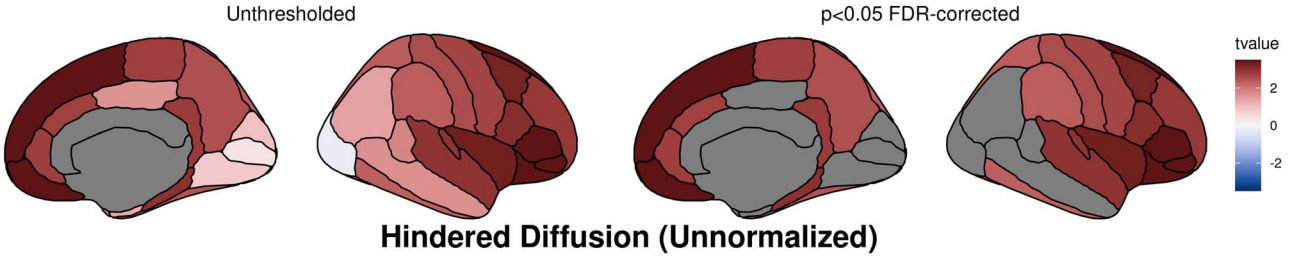

Fig. 2. Regional associations of LC_{CNR} with unnormalized hindered diffusion. Locus coeruleus contrast-to-noise ratio (LC_{CNR}) was used as an independent variable with unnormalized total hindered diffusion as dependent variable across ROIs defined by the Desikan-Killiany atlas. Left and right hemispheres were averaged for each ROI. Unthresholded t-value maps are presented on the left, and significant regions ($P < 0.05$) surviving FDR-correction are presented on the right for each metric. Visualizations created with the R package *ggseg* (Mowinckel and Vidal-Piñeiro 2020).

significant, indicating that these relationships were independent of each other (Supplemental Fig. S4).

Discussion

We found that higher LC_{CNR}, a putative measure of LC structural integrity, was related to differences in cortical microstructure in multiple regions as indexed by the RSI metrics of total hindered and free water signal fractions. Assessing LC integrity is particularly relevant for this sample of community-dwelling individuals in early old age as this structure accrues abnormal tau pathology early in life (Braak et al. 2011; Harley et al. 2021) and is highly affected throughout the course of

Table 1. Results of regression analyses testing associations between LC_{CNR} and normalized restriction spectrum imaging measures.

Region	Estimate	SE	t-value	P
Cortical thickness				
Fusiform	0.114	0.049	2.316	0.021
Frontal pole	0.100	0.049	2.044	0.042
RSI: Total restricted diffusion				
Rostral anterior cingulate	−0.115	0.046	−2.516	0.012
Caudal anterior cingulate	−0.106	0.048	−2.231	0.026
RSI: Total hindered diffusion				
Medial orbitofrontal	0.158	0.048	3.262	**0.001**
Lateral orbitofrontal	0.155	0.048	3.252	**0.001**
Parahippocampal	0.145	0.049	2.950	**0.003**
Insula	0.135	0.047	2.895	**0.004**
Isthmus cingulate	0.135	0.048	2.822	**0.005**
Pars triangularis	0.132	0.048	2.777	**0.006**
Frontal pole	0.135	0.049	2.762	**0.006**
Fusiform gyrus	0.133	0.048	2.745	**0.006**
Pars orbitalis	0.131	0.048	2.707	**0.007**
Temporal pole	0.133	0.050	2.660	**0.008**
Inferior temporal	0.119	0.047	2.525	**0.012**
Caudal middle frontal	0.114	0.048	2.373	**0.018**
Superior temporal	0.107	0.046	2.330	**0.020**
Supramarginal	0.107	0.046	2.327	0.020
Entorhinal	0.110	0.049	2.224	0.027
Postcentral	0.100	0.047	2.124	0.034
Middle temporal	0.098	0.046	2.116	0.035
Precuneus	0.094	0.046	2.069	0.039
Superior frontal	0.096	0.047	2.063	0.040
Rostral middle frontal	0.094	0.047	1.998	0.046
RSI: Isotropic-free water				
Medial orbitofrontal	−0.155	0.048	−3.220	**0.001**
Lateral orbitofrontal	−0.147	0.048	−3.077	**0.002**
Parahippocampal	−0.142	0.048	−2.951	**0.003**
Frontal pole	−0.143	0.049	−2.938	**0.003**
Pars triangularis	−0.139	0.047	−2.936	**0.004**
Insula	−0.131	0.046	−2.820	**0.005**
Isthmus cingulate	−0.125	0.048	−2.625	**0.009**
Caudal middle frontal	−0.121	0.048	−2.535	**0.012**
Temporal pole	−0.126	0.050	−2.532	**0.012**
Fusiform	−0.117	0.048	−2.435	**0.015**
Supramarginal	−0.109	0.046	−2.355	0.019
Inferior temporal	−0.107	0.048	−2.243	0.025
Postcentral	−0.108	0.048	−2.242	0.025
Superior temporal	−0.103	0.047	−2.205	0.028
Pars orbitalis	−0.103	0.048	−2.144	0.033

Coefficients for the LC_{CNR} are listed below. Cortical thickness and normalized restriction spectrum imaging (RSI) metrics from each ROI were used as dependent variables. RSI measures including total restricted, total hindered, and free water signal fractions. Left and right hemispheres were averaged for each ROI defined by the Desikan-Killiany atlas. All nominally significant ($P < 0.05$) associations are presented. P-values surviving FDR-correction are highlighted in bold.

AD (Ehrenberg et al. 2017; Kelly et al. 2017; Theofilas et al. 2017). Linking LC_{CNR} to other neural correlates provides important context to clarify whether individual differences are benign or suggest the influence of pathogenic processes. Microstructural differences were found in regions overlapping with the fronto-parietal and salience networks. The LC is densely connected to these regions (Aston-Jones et al. 2002; Samuels and Szabadi 2008), and prior studies have found that activity in these regions is correlated with both activity in the LC (Raizada and Poldrack 2007; Jacobs et al. 2018) and with pupil dilation (Murphy et al. 2011; Murphy et al. 2014; Elman et al. 2017a), a physiological response tightly linked to LC activity (Rajkowski et al. 1994; Gilzenrat et al. 2010).

Although the associations that survived correction are more extensive for the hindered signal fraction than free water, an inspection of the unthresholded results makes it clear that the patterns are quite similar. Hindered and restricted diffusion are often interpreted as reflecting extra- vs intra-cellular compartments. This is generally the case in white matter, but in gray matter it may be more accurately interpreted as extra- vs intra-neurite (White et al. 2013a; Palombo et al. 2020; Reas et al. 2020). Thus, in gray matter, hindered diffusion likely reflects signal from extra-cellular space, but also large cell bodies, glia, astrocytes, and unmyelinated processes through which water exchanges relatively freely. The general finding in the current study is that higher LC_{CNR} (greater structural integrity) is associated with a greater

Table 2. Results of regression analyses testing associations between LC_{CNR} and unnormalized hindered diffusion.

Region	Estimate	SE	*t*-value	*P*
RSI: Total hindered diffusion				
Lateral orbitifrontal	0.196	0.045	4.337	**0.000**
Medial orbitofrontal	0.199	0.047	4.261	**0.000**
Superior frontal	0.168	0.044	3.785	**0.000**
Pars orbitalis	0.165	0.044	3.783	**0.000**
Pars triangularis	0.154	0.044	3.534	**0.000**
Insula	0.146	0.044	3.297	**0.001**
Caudal middle frontal	0.150	0.046	3.248	**0.001**
Pars opercularis	0.134	0.044	3.039	**0.003**
Parahippocampal	0.145	0.049	2.978	**0.003**
Superior temporal	0.126	0.043	2.951	**0.003**
Transverse temporal	0.132	0.045	2.947	**0.003**
Rostral middle frontal	0.129	0.045	2.865	**0.004**
Isthmus cingulate	0.126	0.044	2.836	**0.005**
Rostral anterior cingulate	0.127	0.046	2.784	**0.006**
Paracentral	0.123	0.045	2.766	**0.006**
Caudal anterior cingulate	0.129	0.047	2.751	**0.006**
Precentral	0.122	0.045	2.704	**0.007**
Postcentral	0.117	0.046	2.574	**0.010**
Precuneus	0.102	0.040	2.530	**0.012**
Fusiform	0.108	0.044	2.472	**0.014**
Superior parietal	0.103	0.044	2.350	**0.019**
Supramarginal	0.104	0.044	2.338	**0.020**
Inferior temporal	0.098	0.043	2.311	**0.021**

Coefficients for the LC_{CNR} are listed below. Unnormalized hindered diffusion from each ROI was used as the dependent variable. Left and right hemispheres were averaged for each ROI defined by the Desikan-Killiany atlas. All nominally significant ($P < 0.05$) associations are presented. *P*-values surviving FDR-correction are highlighted in bold.

signal fraction in the hindered compartment and corresponding lower signal fraction from free water. Analysis of unnormalized metrics suggest that this pattern of results was primarily driven by differences in hindered diffusion. This may suggest that greater rostral/middle LC integrity is associated with greater microstructural integrity in the cortex as reflected by more signal coming from large cell bodies and glial cells. In contrast, lower LC integrity may be associated with a breakdown in cytoarchitectural barriers and a subsequent encroachment of surrounding CSF, resulting in a larger free water signal fraction. In this case, differences in RSI metrics could be considered to reflect subtle forms of atrophy that are cumulatively expected to contribute to the macrostructural changes measured by cortical thickness. However, longitudinal assessment will be necessary to determine whether these differences reflect change in structure as opposed to long-standing differences.

A recent study found that LC_{CNR} was associated with cortical thickness in a similar set of regions as those found in the current study (Bachman et al. 2021). We did not find significant associations with cortical thickness. That may be due to the relatively younger age of our sample and truncated range at the high end, which would be consistent with our hypothesis that dMRI might be more sensitive to early changes than standard T1-weighted images. Other studies have found that both conventional and advanced diffusion metrics demonstrate age and disease-related effects in the absence of or after adjusting for effects detected by macrostructural measures of cortical thickness and volume (Fellgiebel et al. 2006; Scola et al. 2010; Douaud et al. 2013; Parker et al. 2018; Vogt et al. 2020; Weston et al. 2020). In the VETSA sample we found that cortical MD at baseline (mean age 56) predicted incident MCI 12 years later while cortical thickness did not (Williams et al. 2021). Cortical thickness was associated with prevalent MCI in that study, again suggesting that dMRI detects microstructural differences that precede macrostructural ones. Advanced diffusion techniques have been found to be even more sensitive than conventional DTI in detecting AD-related differences (Fu et al. 2020). This may be due to the ability of methods such as RSI to better characterize underlying architectural features (e.g. by resolving crossing fibers and separating diffusion compartments) that may otherwise combine in ways that obscure subtle differences. However, consistent with the Bachman et al. (2021) study, effects among older adults were specific to more rostral portions of the LC. Taken together, these findings suggest that lower rostral/middle LC_{CNR} is associated with structural differences in connected brain regions. This may reflect widespread neurodegenerative processes that affect the brain more globally. We did find that hippocampal volume was also associated with hindered diffusion. However, these associations were independent of those with the LC. Multiple factors likely contribute to individual differences in cortical microstructure, and it may be that the associations with hippocampal volume and LC integrity reflect different underlying processes.

Although we do not have measures of AD pathology (i.e. amyloid and tau), there is evidence to suggest that lower LC_{CNR} is linked to AD pathologic processes and not

solely a function of normal aging. Autopsy studies find abnormal tau in the LC is common by midlife (Braak et al. 2011; Braak and Del Tredici 2011). LC_{CNR} has been shown to decline at older ages, but a recent study incorporating imaging and autopsy data found that this can largely be explained by the presence of AD pathology (Jacobs et al. 2021). We previously found that lower LC_{CNR} is related to increased odds of amnestic mild cognitive impairment and lower memory performance (among other domains) (Elman et al. 2021), and that diagnosis of amnestic mild cognitive impairment is associated with higher AD polygenic risk (Logue et al. 2019). The study by Jacobs et al. (2021) showed similar results, and further found that this association was mediated by entorhinal cortex tau burden. The authors of that study suggest that LC_{CNR} may serve as a proxy for early accumulation of abnormal tau.

The association between LC integrity and cortical microstructure may reflect correlated outcomes of a common cause. It may also be that LC integrity indirectly contributes to the integrity of cortical microstructure, and these possibilities are not mutually exclusive. Such a relationship is most likely to occur through increased neuroinflammation and a decline in neuroprotective processes (Robertson 2013; Mather and Harley 2016; Weinshenker 2018; Giorgi et al. 2019). Disrupted functioning of the LC-NE system can promote the development of core AD pathologies of amyloid (Heneka et al. 2006; Kalinin et al. 2007; Jardanhazi-Kurutz et al. 2010; Chen et al. 2014) and tau (Zhang et al. 2020). The LC may confer neuroprotective effects against these pathologies by expressing high levels of neuropeptides such as somatostatin and galanin (Weinshenker and Holmes 2016; Paik et al. 2021). Additionally, activation of β-adrenergic receptors facilitates downstream activation of the cAMP pathway which regulates expression of inflammatory and growth factors such as BDNF that are important for cell survival (Counts and Mufson 2010). Thus, when levels of NE are depleted the inflammatory response to Aβ and tau may become more toxic, resulting in heightened neurodegeneration (Heneka et al. 2002; Jardanhazi-Kurutz et al. 2011; Chalermpalanupap et al. 2017; Matchett et al. 2021). Elevated neuronal activity across the lifespan may contribute to increased release of Aβ (Jagust and Mormino 2011). The LC-NE system acts as a neuromodulator that increases efficiency of cortical activity. In the absence of proper modulation, there may be inefficient processes requiring heightened activity and a subsequent increase in Aβ production. LC dysfunction thus contributes to multiple processes with bidirectional relationships that exacerbate each other and further neurodegenerative processes.

There are several limitations that should be noted. First, the VETSA is an all-male, primarily white sample; results may not generalize to other samples. The lack of female participants is potentially important because estrogen is a key regulator of the LC-noradrenergic system, so LC dysfunction may have a larger impact in women following menopause when estrogen levels drop substantially (Luckey et al. 2021). This could potentially explain the lack of association with cortical thickness; however, the study by Bachman et al. (2021) did not find that this association differed by sex. Further study investigating the modulatory impact of sex is important to understanding the impacts of LC-noradrenergic system dysfunction. Other studies have used different methods to extract LC_{CNR}, such as taking the maximum value instead of mean from each ROI, and choosing the slice with the maximum LC_{CNR} instead of selecting based on location. We found taking the maximum or mean value of each ROI resulted in almost identical LC_{CNR}. Selecting slices based on peak LC_{CNR} also resulted in similar, albeit weaker associations. This may reflect variability in which region is being examined across participants which, given the apparent spatial specificity of effects in the LC, could explain differences in the strength of subsequent associations. These analyses are cross-sectional, so it is possible that the associations found here represent long-standing individual differences rather than the products of neurodegenerative processes. The impact of CSF partial voluming is of particular importance when examining diffusion in cortical gray matter (Henf et al. 2018; Fukutomi et al. 2019). Our method of projecting diffusion metrics using weighted averages of multiple samples attenuates these effects to an extent. Yet, because the normalized metrics are signal fractions summing to 1, it is possible that associations with the hindered component are driven by partial voluming as reflected by increased free water signal fractions. However, examining the unnormalized metrics provides evidence that the results found here were driven primarily by the hindered diffusion component. The source of hindered diffusion signal is also less clear than the restricted or free water compartments. It likely includes signal from the extracellular space as well as large cell bodies and glia. Additional histological evidence will be needed to more accurately link differences in hindered diffusion within cortical GM to specific cytoarchitectural features.

Identifying early signs of declines in brain health will be critical for efforts to prevent cognitive and functional decline in aging and disease. This may be particularly important for early identification of AD given it high prevalence and early involvement of the LC. Dysfunction of the LC-NE system may arise from global neurodegenerative processes, but it can also contribute to the progression of such processes through increased inflammation and reduced neuroprotective effects. Advanced diffusion techniques such as RSI may provide sensitive measures necessary to detect subtle differences in cortical microstructure that precede macrostructural change. The association between these two measures suggests these differences reflect neurodegenerative processes and support their use in identifying age and early disease-related decline in brain health.

Supplementary Material

Supplementary material can be found at *Cerebral Cortex* online.

Funding

The National Institute on Aging at the National Institutes of Health (grant numbers R01 AG022381, R01 AG050595, R01 AG062483, R01 AG056410, R01 AG059329, P01 AG055367, and K01 AG063805).

Notes

The content of this manuscript is the responsibility of the authors and does not represent official views of NIA/NIH, or the Veterans' Administration. Numerous organizations provided invaluable assistance in the conduct of the VET Registry, including: US Department of Veterans Affairs, Department of Defense; National Personnel Records Center, National Archives and Records Administration; Internal Revenue Service; National Opinion Research Center; National Research Council, National Academy of Sciences; the Institute for Survey Research, Temple University. The authors gratefully acknowledge the continued cooperation of the twins and the efforts of many staff members. *Conflict of Interest*: L.K. McEvoy has stock options in CorTechs Laboratories, Inc. A.M. Dale is a Founder of and holds equity in CorTechs Laboratories, Inc, and serves on its Scientific Advisory Board. He is a member of the Scientific Advisory Board of Human Longevity, Inc and receives funding through research agreements with General Electric Healthcare and Medtronic, Inc. The terms of these arrangements have been reviewed and approved by University of California, San Diego in accordance with its conflict of interest policies. The other authors report no conflict.

References

Aston-Jones G, Cohen JD. 2005. An integrative theory of locus coeruleus-norepinephrine function: adaptive gain and optimal performance. *Annu Rev Neurosci*. 28:403–450.

Aston-Jones G, Rajkowski J, Kubiak P, Alexinsky T. 1994. Locus coeruleus neurons in monkey are selectively activated by attended cues in a vigilance task. *J Neurosci*. 14:4467–4480.

Aston-Jones G, Rajkowski J, Lu W, Zhu Y, Cohen JD, Morecraft RJ. 2002. Prominent projections from the orbital prefrontal cortex to the locus coeruleus in monkey. *Soc. Neurosci. Abstr*. 2002:86–89.

Bachman SL, Dahl MJ, Werkle-Bergner M, Duzel S, Forlim CG, Lindenberger U, Kuhn S, Mather M. 2021. Locus coeruleus MRI contrast is associated with cortical thickness in older adults. *Neurobiol Aging*. 100:72–82.

Bates D, Machler M, Bolker BM, Walker SC. 2015. Fitting linear mixed-effects models using lme4. *J Stat Softw*. 67:1–48.

Berridge CW, Waterhouse BD. 2003. The locus coeruleus-noradrenergic system: modulation of behavioral state and state-dependent cognitive processes. *Brain Res Brain Res Rev*. 42: 33–84.

Betts MJ, Cardenas-Blanco A, Kanowski M, Spottke A, Teipel SJ, Kilimann I, Jessen F, Duzel E. 2019a. Locus coeruleus MRI contrast is reduced in Alzheimer's disease dementia and correlates with CSF Abeta levels. *Alzheimers Dement (Amst)*. 11:281–285.

Betts MJ, Kirilina E, Otaduy MCG, Ivanov D, Acosta-Cabronero J, Callaghan MF, Lambert C, Cardenas-Blanco A, Pine K, Passamonti L, et al. 2019b. Locus coeruleus imaging as a biomarker for noradrenergic dysfunction in neurodegenerative diseases. *Brain*. 142:2558–2571.

Bondareff W, Mountjoy CQ, Roth M, Rossor MN, Iversen LL, Reynolds GP, Hauser DL. 1987. Neuronal degeneration in locus ceruleus and cortical correlates of Alzheimer disease. *Alzheimer Dis Assoc Disord*. 1:256–262.

Braak H, Del Tredici K. 2011. The pathological process underlying Alzheimer's disease in individuals under thirty. *Acta Neuropathol*. 121:171–181.

Braak H, Thal DR, Ghebremedhin E, Del Tredici K. 2011. Stages of the pathologic process in Alzheimer disease: age categories from 1 to 100 years. *J Neuropathol Exp Neurol*. 70:960–969.

Breton-Provencher V, Drummond GT, Sur M. 2021. Locus coeruleus norepinephrine in learned behavior: anatomical modularity and spatiotemporal integration in targets. *Front Neural Circuits*. 15:638007.

Chalermpalanupap T, Schroeder JP, Rorabaugh JM, Liles LC, Lah JJ, Levey AI, Weinshenker D. 2018. Locus coeruleus ablation exacerbates cognitive deficits, neuropathology, and lethality in P301S tau transgenic mice. *J Neurosci*. 38:74–92.

Chang H, Fitzpatrick JM. 1992. A technique for accurate magnetic resonance imaging in the presence of field inhomogeneities. *IEEE Trans Med Imaging*. 11:319–329.

Chen MJ, Russo-Neustadt AA. 2007. Nitric oxide signaling participates in norepinephrine-induced activity of neuronal intracellular survival pathways. *Life Sci*. 81:1280–1290.

Chen Y, Peng Y, Che P, Gannon M, Liu Y, Li L, Bu G, van Groen T, Jiao K, Wang Q. 2014. Alpha(2A) adrenergic receptor promotes amyloidogenesis through disrupting APP-SorLA interaction. *Proc Natl Acad Sci U S A*. 111:17296–17301.

Counts SE, Mufson EJ. 2010. Noradrenaline activation of neurotrophic pathways protects against neuronal amyloid toxicity. *J Neurochem*. 113:649–660.

Dahl MJ, Mather M, Duzel S, Bodammer NC, Lindenberger U, Kuhn S, Werkle-Bergner M. 2019. Rostral locus coeruleus integrity is associated with better memory performance in older adults. *Nat Hum Behav*. 3:1203–1214.

Dale AM, Fischl B, Sereno MI. 1999. Cortical surface-based analysis. I. Segmentation and surface reconstruction. *NeuroImage*. 9:179–194.

Desikan RS, Segonne F, Fischl B, Quinn BT, Dickerson BC, Blacker D, Buckner RL, Dale AM, Maguire RP, Hyman BT, et al. 2006. An automated labeling system for subdividing the human cerebral cortex on MRI scans into gyral based regions of interest. *NeuroImage*. 31: 968–980.

Douaud G, Menke RAL, Gass A, Monsch AU, Rao A, Whitcher B, Zamboni G, Matthews PM, Sollberger M, Smith S. 2013. Brain microstructure reveals early abnormalities more than two years prior to clinical progression from mild cognitive impairment to Alzheimer's disease. *J Neurosci*. 33:2147–2155.

Ehrenberg AJ, Nguy AK, Theofilas P, Dunlop S, Suemoto CK, Di Lorenzo Alho AT, Leite RP, Diehl Rodriguez R, Mejia MB, Rub U, et al. 2017. Quantifying the accretion of hyperphosphorylated tau in the locus coeruleus and dorsal raphe nucleus: the pathological building blocks of early Alzheimer's disease. *Neuropathol Appl Neurobiol*. 43:393–408.

Elman JA, Panizzon MS, Hagler DJ Jr, Eyler LT, Granholm EL, Fennema-Notestine C, Lyons MJ, McEvoy LK, Franz CE, Dale AM, et al. 2017a. Task-evoked pupil dilation and BOLD

variance as indicators of locus coeruleus dysfunction. *Cortex*. 97: 60–69.

Elman JA, Panizzon MS, Hagler DJ Jr, Fennema-Notestine C, Eyler LT, Gillespie NA, Neale MC, Lyons MJ, Franz CE, McEvoy LK, et al. 2017b. Genetic and environmental influences on cortical mean diffusivity. *NeuroImage*. 146:90–99.

Elman JA, Puckett OK, Beck A, Fennema-Notestine C, Cross LK, Dale AM, Eglit GML, Eyler LT, Gillespie NA, Granholm EL, et al. 2021. MRI-assessed locus coeruleus integrity is heritable and associated with multiple cognitive domains, mild cognitive impairment, and daytime dysfunction. *Alzheimers Dement*. 17:1017–1025.

Feinstein DL, Heneka MT, Gavrilyuk V, Dello Russo C, Weinberg G, Galea E. 2002. Noradrenergic regulation of inflammatory gene expression in brain. *Neurochem Int*. 41:357–365.

Fellgiebel A, Dellani PR, Greverus D, Scheurich A, Stoeter P, Müller MJ. 2006. Predicting conversion to dementia in mild cognitive impairment by volumetric and diffusivity measurements of the hippocampus. *Psychiatry Res Neuroimaging*. 146:283–287.

Fischl B, Dale AM. 2000. Measuring the thickness of the human cerebral cortex from magnetic resonance images. *Proc Natl Acad Sci U S A*. 97:11050–11055.

Fischl B, Sereno MI, Dale AM. 1999. Cortical surface-based analysis. II: inflation, flattening, and a surface-based coordinate system. *NeuroImage*. 9:195–207.

Fischl B, Salat DH, Busa E, Albert M, Dieterich M, Haselgrove C, van der Kouwe A, Killiany R, Kennedy D, Klaveness S, et al. 2002. Whole brain segmentation: automated labeling of neuroanatomical structures in the human brain. *Neuron*. 33:341–355.

Fischl B, Salat DH, van der Kouwe AJ, Makris N, Segonne F, Quinn BT, Dale AM. 2004a. Sequence-independent segmentation of magnetic resonance images. *NeuroImage*. 23(Suppl 1):S69–S84.

Fischl B, van der Kouwe A, Destrieux C, Halgren E, Segonne F, Salat DH, Busa E, Seidman LJ, Goldstein J, Kennedy D, et al. 2004b. Automatically parcellating the human cerebral cortex. *Cereb Cortex*. 14:11–22.

Fu X, Shrestha S, Sun M, Wu Q, Luo Y, Zhang X, Yin J, Ni H. 2020. Microstructural White matter alterations in mild cognitive impairment and Alzheimer's disease: study based on neurite orientation dispersion and density imaging (NODDI). *Clin Neuroradiol*. 30:569–579.

Fukutomi H, Glasser MF, Murata K, Akasaka T, Fujimoto K, Yamamoto T, Autio JA, Okada T, Togashi K, Zhang H, et al. 2019. Diffusion tensor model links to neurite orientation dispersion and density imaging at high b-value in cerebral cortical Gray matter. *Sci Rep*. 9:12246.

German DC, White CL, Sparkman DR. 1987. Alzheimer's disease: neurofibrillary tangles in nuclei that project to the cerebral cortex. *Neuroscience*. 21:305–312.

German DC, Manaye KF, White CL, Woodward DJ, McIntire DD, Smith WK, Kalaria RN, Mann DMA. 1992. Disease-specific patterns of locus coeruleus cell loss. *Ann Neurol*. 32:667–676.

Gilzenrat MS, Nieuwenhuis S, Jepma M, Cohen JD. 2010. Pupil diameter tracks changes in control state predicted by the adaptive gain theory of locus coeruleus function. *Cogn Affect Behav Neurosci*. 10: 252–269.

Giorgi FS, Saccaro LF, Galgani A, Busceti CL, Biagioni F, Frati A, Fornai F. 2019. The role of locus coeruleus in neuroinflammation occurring in Alzheimer's disease. *Brain Res Bull*. 153: 47–58.

Grudzien A, Shaw P, Weintraub S, Bigio E, Mash DC, Mesulam MM. 2007. Locus coeruleus neurofibrillary degeneration in aging, mild cognitive impairment and early Alzheimer's disease. *Neurobiol Aging*. 28:327–335.

Hagler DJ Jr, Ahmadi ME, Kuperman J, Holland D, McDonald CR, Halgren E, Dale AM. 2009. Automated white-matter tractography using a probabilistic diffusion tensor atlas: application to temporal lobe epilepsy. *Hum Brain Mapp*. 30:1535–1547.

Hagler DJ Jr, Hatton S, Cornejo MD, Makowski C, Fair DA, Dick AS, Sutherland MT, Casey BJ, Barch DM, Harms MP, et al. 2019. Image processing and analysis methods for the adolescent brain cognitive development study. *NeuroImage*. 202:116091.

Hammerer D, Callaghan MF, Hopkins A, Kosciessa J, Betts M, Cardenas-Blanco A, Kanowski M, Weiskopf N, Dayan P, Dolan RJ, et al. 2018. Locus coeruleus integrity in old age is selectively related to memories linked with salient negative events. *Proc Natl Acad Sci U S A*. 115(9):2228–2233.

Harley CW, Walling SG, Yuan Q, Martin GM. 2021. The 'a, b, c's of pretangle tau and their relation to aging and the risk of Alzheimer's disease. *Semin Cell Dev Biol*. 116:125–134.

Heneka MT, Galea E, Gavriluyk V, Dumitrescu-Ozimek L, Daeschner J, O'Banion MK, Weinberg G, Klockgether T, Feinstein DL. 2002. Noradrenergic depletion potentiates beta -amyloid-induced cortical inflammation: implications for Alzheimer's disease. *J Neurosci*. 22:2434–2442.

Heneka MT, Ramanathan M, Jacobs AH, Dumitrescu-Ozimek L, Bilkei-Gorzo A, Debeir T, Sastre M, Galldiks N, Zimmer A, Hoehn M, et al. 2006. Locus ceruleus degeneration promotes Alzheimer pathogenesis in amyloid precursor protein 23 transgenic mice. *J Neurosci*. 26:1343–1354.

Heneka MT, Nadrigny F, Regen T, Martinez-Hernandez A, Dumitrescu-Ozimek L, Terwel D, Jardanhazi-Kurutz D, Walter J, Kirchhoff F, Hanisch UK, et al. 2010. Locus ceruleus controls Alzheimer's disease pathology by modulating microglial functions through norepinephrine. *Proc Natl Acad Sci U S A*. 107:6058–6063.

Henf J, Grothe MJ, Brueggen K, Teipel S, Dyrba M. 2018. Mean diffusivity in cortical gray matter in Alzheimer's disease: the importance of partial volume correction. *Neuroimage Clin*. 17:579–586.

Holland D, Kuperman JM, Dale AM. 2010. Efficient correction of inhomogeneous static magnetic field-induced distortion in Echo planar imaging. *NeuroImage*. 50:175–183.

Jacobs HIL, Muller-Ehrenberg L, Priovoulos N, Roebroeck A. 2018. Curvilinear locus coeruleus functional connectivity trajectories over the adult lifespan: a 7T MRI study. *Neurobiol Aging*. 69: 167–176.

Jacobs HIL, Becker JA, Kwong K, Engels-Dominguez N, Prokopiou PC, Papp KV, Properzi M, Hampton OL, d'Oleire Uquillas F, Sanchez JS, et al. 2021. In vivo and neuropathology data support locus coeruleus integrity as indicator of Alzheimer's disease pathology and cognitive decline. *Sci Transl Med*. 13:eabj2511.

Jagust WJ, Mormino EC. 2011. Lifespan brain activity, β-amyloid, and Alzheimer's disease. *Trends Cogn Sci*. 15:520–526.

Jak AJ, Bondi MW, Delano-Wood L, Wierenga C, Corey-Bloom J, Salmon DP, Delis DC. 2009. Quantification of five neuropsychological approaches to defining mild cognitive impairment. *Am J Geriatric Psychiat: Off J Am Assoc Geriatric Psychiatry*. 17:368–375.

Jardanhazi-Kurutz D, Kummer MP, Terwel D, Vogel K, Dyrks T, Thiele A, Heneka MT. 2010. Induced LC degeneration in APP/PS1 transgenic mice accelerates early cerebral amyloidosis and cognitive deficits. *Neurochem Int*. 57:375–382.

Jardanhazi-Kurutz D, Kummer MP, Terwel D, Vogel K, Thiele A, Heneka MT. 2011. Distinct adrenergic system changes and neuroinflammation in response to induced locus ceruleus degeneration in APP/PS1 transgenic mice. *Neuroscience*. 176:396–407.

Jovicich J, Czanner S, Greve D, Haley E, van der Kouwe A, Gollub R, Kennedy D, Schmitt F, Brown G, Macfall J, et al. 2006. Reliability

in multi-site structural MRI studies: effects of gradient non-linearity correction on phantom and human data. *NeuroImage*. 30: 436–443.

Kalinin S, Gavrilyuk V, Polak PE, Vasser R, Zhao J, Heneka MT, Feinstein DL. 2007. Noradrenaline deficiency in brain increases beta-amyloid plaque burden in an animal model of Alzheimer's disease. *Neurobiol Aging*. 28:1206–1214.

Kaup AR, Toomey R, Bangen KJ, Delano-Wood L, Yaffe K, Panizzon MS, Lyons MJ, Franz CE, Kremen WS. 2019. Interactive effect of traumatic brain injury and psychiatric symptoms on cognition among late middle-aged men: findings from the Vietnam era twin study of aging. *J Neurotrauma*. 36:338–347.

Kelberman M, Keilholz S, Weinshenker D. 2020. What's that (blue) spot on my MRI? Multimodal neuroimaging of the locus coeruleus in neurodegenerative disease. *Front Neurosci*. 14:583421. doi: https://doi.org/10.3389/fnins.2020.583421.

Kelly SC, He B, Perez SE, Ginsberg SD, Mufson EJ, Counts SE. 2017. Locus coeruleus cellular and molecular pathology during the progression of Alzheimer's disease. *Acta Neuropathol Commun*. 5:8.

Keren NI, Taheri S, Vazey EM, Morgan PS, Granholm AC, Aston-Jones GS, Eckert MA. 2015. Histologic validation of locus coeruleus MRI contrast in post-mortem tissue. *NeuroImage*. 113:235–245.

Kremen WS, Prom-Wormley E, Panizzon MS, Eyler LT, Fischl B, Neale MC, Franz CE, Lyons MJ, Pacheco J, Perry ME, et al. 2010. Genetic and environmental influences on the size of specific brain regions in midlife: the VETSA MRI study. *NeuroImage*. 49: 1213–1223.

Kremen WS, Franz CE, Lyons MJ. 2019. Current status of the Vietnam era twin study of aging (VETSA). *Twin Res Hum Genet*. 22:783–787.

Kuznetsova A, Brockhoff PB, Christensen RHB. 2017. lmerTest package: tests in linear mixed effects models. *J Stat Softw*. 82:1–26.

Li J, Ji L. 2005. Adjusting multiple testing in multilocus analyses using the eigenvalues of a correlation matrix. *Heredity*. 95:221–227.

Liu KY, Marijatta F, Hammerer D, Acosta-Cabronero J, Duzel E, Howard RJ. 2017. Magnetic resonance imaging of the human locus coeruleus: a systematic review. *Neurosci Biobehav Rev*. 83:325–355.

Logue MW, Panizzon MS, Elman JA, Gillespie NA, Hatton SN, Gustavson DE, Andreassen OA, Dale AM, Franz CE, Lyons MJ, et al. 2019. Use of an Alzheimer's disease polygenic risk score to identify mild cognitive impairment in adults in their 50s. *Mol Psychiatry*. 24:421–430.

Luckey AM, Robertson IH, Lawlor B, Mohan A, Vanneste S. 2021. Sex differences in locus coeruleus: a heuristic approach that may explain the increased risk of Alzheimer's disease in females. *Journal of Alzheimer's Disease: JAD*. 83:505–522.

Lyons MJ, York TP, Franz CE, Grant MD, Eaves LJ, Jacobson KC, Schaie KW, Panizzon MS, Boake C, Xian H, et al. 2009. Genes determine stability and the environment determines change in cognitive ability during 35 years of adulthood. *Psychol Sci*. 20:1146–1152.

Lyons MJ, Panizzon MS, Liu W, McKenzie R, Bluestone NJ, Grant MD, Franz CE, Vuoksimaa EP, Toomey R, Jacobson KC, et al. 2017. A longitudinal twin study of general cognitive ability over four decades. *Dev Psychol*. 53:1170–1177.

Matchett BJ, Grinberg LT, Theofilas P, Murray ME. 2021. The mechanistic link between selective vulnerability of the locus coeruleus and neurodegeneration in Alzheimer's disease. *Acta Neuropathol*. 141(5):631–650.

Mather M, Harley CW. 2016. The locus coeruleus: essential for maintaining cognitive function and the aging brain. *Trends Cogn Sci*. 20: 214–226. doi: https://doi.org/10.1016/j.tics.2016.01.001.

Mather M, Clewett D, Sakaki M, Harley CW. 2016. Norepinephrine ignites local hot spots of neuronal excitation: how arousal amplifies selectivity in perception and memory. *Behav Brain Sci*. 1–100.

Morgan PS, Bowtell RW, McIntyre DJ, Worthington BS. 2004. Correction of spatial distortion in EPI due to inhomogeneous static magnetic fields using the reversed gradient method. *J Magn Reson Imaging*. 19:499–507.

Mowinckel AM, Vidal-Piñeiro D. 2020. Visualization of brain statistics with R packages ggseg and ggseg3d. *Adv Methods Pract Psychol Sci*. 3:466–483.

Murphy PR, Robertson IH, Balsters JH, O'Connell RG. 2011. Pupillometry and P3 index the locus coeruleus–noradrenergic arousal function in humans. *Psychophysiology*. 48:1532–1543.

Murphy PR, O'Connell RG, O'Sullivan M, Robertson IH, Balsters JH. 2014. Pupil diameter covaries with BOLD activity in human locus coeruleus: pupil diameter and locus coeruleus activity. *Hum Brain Mapp*. 35:4140–4154.

Paik S, Somvanshi RK, Oliveira HA, Zou S, Kumar U. 2021. Somatostatin ameliorates beta-amyloid-induced cytotoxicity via the regulation of CRMP2 phosphorylation and calcium homeostasis in SH-SY5Y cells. *Biomedicine*. 9:27.

Palombo M, Ianus A, Guerreri M, Nunes D, Alexander DC, Shemesh N, Zhang H. 2020. SANDI: a compartment-based model for non-invasive apparent soma and neurite imaging by diffusion MRI. *NeuroImage*. 215:116835.

Parker TD, Slattery CF, Zhang J, Nicholas JM, Paterson RW, Foulkes AJM, Malone IB, Thomas DL, Modat M, Cash DM, et al. 2018. Cortical microstructure in young onset Alzheimer's disease using neurite orientation dispersion and density imaging. *Hum Brain Mapp*. 39:3005–3017.

Priovoulos N, van Boxel SCJ, Jacobs HIL, Poser BA, Uludag K, Verhey FRJ, Ivanov D. 2020. Unraveling the contributions to the neuromelanin-MRI contrast. *Brain Struct Funct*. 225:2757–2774.

R Core Team. 2017. *R: A Language and Environment for Statistical Computing*. Vienna, Austria: R Foundation for Statistical Computing.

Radloff LS. 1977. The CES-D scale: a self-report depression scale for research in the general population. *Appl Psychol Meas*. 1:385–401.

Raizada RD, Poldrack RA. 2007. Challenge-driven attention: interacting frontal and brainstem systems. *Front Hum Neurosci*. 1:3.

Rajkowski J, Kubiak P, Aston-Jones G. 1993. Correlations between locus coeruleus (LC) neural activity, pupil diameter and behavior in monkey support a role of LC in attention. In: *Society for Neuroscience Abstracts*, p. 974.

Rajkowski J, Kubiak P, Aston-Jones G. 1994. Locus coeruleus activity in monkey: phasic and tonic changes are associated with altered vigilance. *Brain Res Bull*. 35:607–616.

Ransohoff RM. 2016. How neuroinflammation contributes to neurodegeneration. *Science*. 353:777–783.

Reas ET, Hagler DJ Jr, White NS, Kuperman JM, Bartsch H, Cross K, Loi RQ, Balachandra AR, Meloy MJ, Wierenga CE, et al. 2017. Sensitivity of restriction spectrum imaging to memory and neuropathology in Alzheimer's disease. *Alzheimers Res Ther*. 9:55.

Reas ET, Hagler DJ, Kuperman JM, Wierenga CE, Galasko D, White NS, Dale AM, Banks SJ, McEvoy LK, Brewer JB. 2020. Associations between microstructure, amyloid, and cognition in amnestic mild cognitive impairment and dementia. *Journal of Alzheimer's Disease: JAD*. 73:347–357.

Robertson IH. 2013. A noradrenergic theory of cognitive reserve: implications for Alzheimer's disease. *Neurobiol Aging*. 34: 298–308.

Samuels ER, Szabadi E. 2008. Functional neuroanatomy of the noradrenergic locus coeruleus: its roles in the regulation of arousal and autonomic function part I: principles of functional organisation. *Curr Neuropharmacol*. 6:235–253.

Sara SJ. 2009. The locus coeruleus and noradrenergic modulation of cognition. *Nat Rev Neurosci*. 10:211–223.

Sara SJ. 2015. Locus coeruleus in time with the making of memories. *Curr Opin Neurobiol*. 35:87–94.

Sara SJ, Bouret S. 2012. Orienting and reorienting: the locus coeruleus mediates cognition through arousal. *Neuron*. 76:130–141.

Sasaki M, Shibata E, Tohyama K, Takahashi J, Otsuka K, Tsuchiya K, Takahashi S, Ehara S, Terayama Y, Sakai A. 2006. Neuromelanin magnetic resonance imaging of locus ceruleus and substantia nigra in Parkinson??S disease. *Neuroreport*. 17:1215–1218.

Schoenborn CA, Heyman KM. 2009. Health characteristics of adults aged 55 years and over: United States, 2004-2007. *Natl Health Stat Rep*. 16:1–31.

Scola E, Bozzali M, Agosta F, Magnani G, Franceschi M, Sormani MP, Cercignani M, Pagani E, Falautano M, Filippi M, et al. 2010. A diffusion tensor MRI study of patients with MCI and AD with a 2-year clinical follow-up. *J Neurol Neurosurg Psychiatry*. 81: 798–805.

Takahashi J, Shibata T, Sasaki M, Kudo M, Yanezawa H, Obara S, Kudo K, Ito K, Yamashita F, Terayama Y. 2015. Detection of changes in the locus coeruleus in patients with mild cognitive impairment and Alzheimer's disease: high-resolution fast spin-echo T1-weighted imaging. *Geriatr Gerontol Int*. 15:334–340.

Theofilas P, Ehrenberg AJ, Dunlop S, Di Lorenzo Alho AT, Nguy A, Leite REP, Rodriguez RD, Mejia MB, Suemoto CK, Ferretti-Rebustini REL, et al. 2017. Locus coeruleus volume and cell population changes during Alzheimer's disease progression: a stereological study in human postmortem brains with potential implication for early-stage biomarker discovery. *Alzheimers Dement*. 13:236–246.

Uhlaner J, Bolanovich DJ. 1952. *Development of Armed Forces Qualification Test and Predecessor Army Screening Tests*, Washington, DC: Army Adjutant Generals Office. pp. 1946–1950. DTIC Document.

Vogt NM, Hunt JF, Adluru N, Dean DC, Johnson SC, Asthana S, Yu JJ, Alexander AL, Bendlin BB. 2020. Cortical microstructural alterations in mild cognitive impairment and Alzheimer's disease dementia. *Cereb Cortex*. 30:2948–2960.

Weinshenker D. 2018. Long road to ruin: noradrenergic dysfunction in neurodegenerative disease. *Trends Neurosci*. 41:211–223.

Weinshenker D, Holmes PV. 2016. Regulation of neurological and neuropsychiatric phenotypes by locus coeruleus-derived galanin. *Brain Res*. 1641:320–337.

Weston PS, Simpson IJ, Ryan NS, Ourselin S, Fox NC. 2015. Diffusion imaging changes in grey matter in Alzheimer's disease: a potential marker of early neurodegeneration. *Alzheimers Res Ther*. 7:47.

Weston PSJ, Poole T, Nicholas JM, Toussaint N, Simpson IJA, Modat M, Ryan NS, Liang Y, Rossor MN, Schott JM, et al. 2020. Measuring cortical mean diffusivity to assess early microstructural cortical change in presymptomatic familial Alzheimer's disease. *Alzheimers Res Ther*. 12:112.

White NS, Leergaard TB, D'Arceuil H, Bjaalie JG, Dale AM. 2013a. Probing tissue microstructure with restriction spectrum imaging: histological and theoretical validation. *Hum Brain Mapp*. 34: 327–346.

White NS, McDonald CR, Farid N, Kuperman JM, Kesari S, Dale AM. 2013b. Improved conspicuity and delineation of high-grade primary and metastatic brain tumors using "restriction spectrum imaging": quantitative comparison with high B-value DWI and ADC. *AJNR Am J Neuroradiol*. 34:958–964, S951.

White NS, McDonald C, Farid N, Kuperman J, Karow D, Schenker-Ahmed NM, Bartsch H, Rakow-Penner R, Holland D, Shabaik A, et al. 2014. Diffusion-weighted imaging in cancer: physical foundations and applications of restriction spectrum imaging. *Cancer Res*. 74:4638–4652.

Whiteneck GG, Cuthbert JP, Corrigan JD, Bogner JA. 2016. Prevalence of self-reported lifetime history of traumatic brain injury and associated disability: a Statewide population-based survey. *J Head Trauma Rehabil*. 31:E55–E62.

Williams ME, Elman JA, McEvoy LK, Andreassen OA, Dale AM, Eglit GML, Eyler LT, Fennema-Notestine C, Franz CE, Gillespie NA, et al. 2021. 12-year prediction of mild cognitive impairment aided by Alzheimer's brain signatures at mean age 56. *Brain Communications*. 3:fcab167. doi: https://doi.org/10.1093/braincomms/fcab167.

Wilson RS, Nag S, Boyle PA, Hizel LP, Yu L, Buchman AS, Schneider JA, Bennett DA. 2013. Neural reserve, neuronal density in the locus ceruleus, and cognitive decline. *Neurology*. 80:1202–1208.

Zhang F, Gannon M, Chen Y, Yan S, Zhang S, Feng W, Tao J, Sha B, Liu Z, Saito T, et al. 2020. Beta-amyloid redirects norepinephrine signaling to activate the pathogenic GSK3beta/tau cascade. *Sci Transl Med*. 12:eaay6931.

Zhuang J, Hrabe J, Kangarlu A, Xu D, Bansal R, Branch CA, Peterson BS. 2006. Correction of eddy-current distortions in diffusion tensor images using the known directions and strengths of diffusion gradients. *J Magn Reson Imaging*. 24:1188–1193.